Chemical Science

ROYAL SOCIETY OF CHEMISTRY

EDGE ARTICLE

Cite this: *Chem. Sci.*, 2024, **15**, 11391

All publication charges for this article have been paid for by the Royal Society of Chemistry

Real-time structural dynamics of the ultrafast solvation process around photo-excited aqueous halides†

Verena Markmann, *[a] Jaysree Pan, [a] Bianca L. Hansen, [a] Morten L. Haubro, [a] Amke Nimmrich, ‡[ab] Philipp Lenzen,§[a] Matteo Levantino, [c] Tetsuo Katayama, [de] Shin-ichi Adachi,[fg] Simone Gorski-Bilke,[h] Friedrich Temps, [h] Asmus O. Dohn, [ai] Klaus B. Møller, [a] Martin M. Nielsen [a] and Kristoffer Haldrup [a]

This work investigates and describes the structural dynamics taking place following charge-transfer-to-solvent photo-abstraction of electrons from I^- and Br^- ions in aqueous solution following single- and 2-photon excitation at 202 nm and 400 nm, respectively. A Time-Resolved X-ray Solution Scattering (TR-XSS) approach with direct sensitivity to the structure of the surrounding solvent as the water molecules adopt a new equilibrium configuration following the electron-abstraction process is utilized to investigate the structural dynamics of solvent shell expansion and restructuring in real-time. The structural sensitivity of the scattering data enables a quantitative evaluation of competing models for the interaction between the nascent neutral species and surrounding water molecules. Taking the I^0–O distance as the reaction coordinate, we find that the structural reorganization is delayed by 0.1 ps with respect to the photoexcitation and completes on a time scale of 0.5–1 ps. On longer time scales we determine from the evolution of the TR-XSS difference signal that I^0: e^- recombination takes place on two distinct time scales of ~20 ps and 100 s of picoseconds. These dynamics are well captured by a simple model of diffusive evolution of the initial photo-abstracted electron population where the charge-transfer-to-solvent process gives rise to a broad distribution of electron ejection distances, a significant fraction of which are in the close vicinity of the nascent halogen atoms and recombine on short time scales.

Received 21st March 2024
Accepted 11th June 2024

DOI: 10.1039/d4sc01912a

rsc.li/chemical-science

1 Introduction

Charge transfer reactions in solution are of high interest for energy transformation, transmission, and storage and understanding the solvation mechanisms involved in such processes enables potential tuneabilities of the solute–solvent bond network and thereby transient state lifetimes. It has been shown that atomic–scale interactions between solute and solvent can directly influence the outcome of chemical reactions[1–4] and biochemical processes.[5–8] In dissociative processes, the surrounding solvent molecules can serve as a cage to confine (photo-) dissociated geminate fragments,[9–11] and through their influence on the position and shape of the potential energy surface solute–solvent interactions have been shown to lead to changes in the lifetime and geometry of photo-excited solute molecules in a range of systems.[12–16] Much progress has been made in studying the interplay between charge state dynamics and the structural dynamics of the solvent *via* time-resolved spectroscopic methods and simulations,[17–20] however, a dearth of experimental probes with both the requisite time- and spatial resolution continues to provide a challenge. Consequently,

[a]*Technical University of Denmark, Anker Engelunds Vej 1, 2800 Lyngby, Denmark. E-mail: vmark@dtu.dk*

[b]*Department of Chemistry and Molecular Biology, University of Gothenburg, Gothenburg, Sweden*

[c]*European Synchrotron Radiation Facility, CS40220, Grenoble 38043 Cedex 9, France*

[d]*Japan Synchrotron Radiation Research Institute, Kouto 1-1-1, Sayo, Hyogo 679-5198, Japan*

[e]*RIKEN SPring-8 Center, 1-1-1 Kouto, Sayo, Hyogo 679-5148, Japan*

[f]*Institute of Materials Structure Science, High Energy Accelerator Research Organization (KEK), 1-1 Oho, Tsukuba, Ibaraki 305-0801, Japan*

[g]*Department of Materials Structure Science, School of High Energy Accelerator Science, 1-1 Oho, Tsukuba, Ibaraki 305-0801, Japan*

[h]*Christian-Albrechts-University Kiel, Olshausenstr. 40, 24098 Kiel, Germany*

[i]*Science Institute, University of Iceland, 107 Reykjavík, Iceland*

† Electronic supplementary information (ESI) available. See DOI: https://doi.org/10.1039/d4sc01912a

‡ Present address: University of Washington, Department of Chemistry, Seattle, WA 98105, USA.

§ Present address: SLAC National Accelerator Laboratory, Menlo Park, California 94025, USA.

a comprehensive mechanistic picture with predictive capabilities regarding solvation dynamics and their influence on chemical reactions has yet to emerge.

Aqueous halides, *e.g.* iodide and bromide, have served as an important set of systems to study the fundamental mechanisms of Charge-Transfer-To-Solvent (CTTS) dynamics. They are highly relevant for solvation studies due to their natural abundance and role in cell biology[21–23] and cloud formation.[24] A prevailing perspective has long been that upon excitation with a photon, the electron abstracted from an aqueous halide first exists in close proximity to its original atom (a so-called contact pair), before it becomes hydrated and dissolves into the solvent as a free electron. This concept was introduced in simulation studies in the 1990s[25–29] and was taken up later in classical Molecular Dynamic (MD) simulations[30,31] and the analysis of experimental results.[32–35]

For example, optical Transient Absorption (TA) studies in the visible spectrum[29,36–38] record the signature of an electron as a spectral feature growing within the first picosecond after excitation and developing to a broad band centered at ~700 nm. Subsequently, this spectral signature decays with two time constants – one assigned to the dissociation of a contact pair into a free electron and a halogen atom (tens of picoseconds) and the other one assigned to the geminate recombination of a free electron with a halogen atom (100–200 ps). Similar to the TA results, two time scales of several tens of picoseconds and ≥100 ps have been reported from the decay of spectra observed in Time-Resolved Photo-Electron Spectroscopy (TRPES) experiments.[39–42] Using TRPES, the electron binding energies were investigated and the exponentially decaying components of the photoelectron intensity profile were associated with the formation of a contact pair and its subsequent dissociation. Further insights into the potential presence and nature of transient species such as $I^0(OH_2)$ have also been suggested by time-resolved X-ray absorption spectroscopy in combination with QM/MM simulations.[35] Very recently the above-mentioned simulation-based studies were further extended by an *ab initio* molecular dynamics simulation study of an iodide surrounded by 256 water molecules.[43] Similar to the simulation results in the earlier works by Pham *et al.* and others, this study also identified the ~0.5 Å expansion of the solvent cage. It was further found that this solvent cage expansion coexists with transiently formed $I–OH_2$ pairs and they utilized a classification approach to shed light on the nature and dynamics of the electron from its formation in a Rydberg state, through contact-pair formation and until it localizes in the bulk solvent.

In the recent experimental work with ultrafast X-ray methods by Vester *et al.*,[44] the existence of the contact pair as a distinct species was brought into question by analysis suggesting an average ejection distance of the photo-abstracted electron of 7.4 ± 1.5 Å, which lies well outside the first solvation shell around an iodine atom. A model with diffusion-driven dynamics of the free electron was shown to be sufficient for fitting the kinetic traces of the iodine 2s–5p transition intensity of X-ray Absorption Near Edge Structure (XANES) data. Thus, the electron could be characterized as free electron directly after photo excitation. From a structural point of view, Vester *et al.* applied Time-resolved X-ray Solution Scattering combined with classical Molecular Dynamics simulations to qualitatively confirm the ~0.5 Å increase in the nearest-neighbour I–O distances and also observed that the onset of this structural change was delayed by ~0.1 ps with respect to the photo excitation event.

Building on the work of Vester *et al.*, our present study utilizes Time-Resolved X-ray Solution Scattering (TR-XSS)[45,46] to investigate the configuration of solvent molecules around the solute after CTTS reactions.[47–49] We employ a model based on classical MD simulations to fit the TR-XSS data, with the interactions between solute and solvent molecules described by using the sum of a Coulomb and a Lennard-Jones (LJ) potential. We investigate the validity of previously proposed LJ potentials by comparing difference signals calculated from the MD simulations to experiments for aqueous halides both before and after photoionisation. Finally, the structural changes around halides are observed for 100 ps to study recombination dynamics as well as to estimate the ejection distance of the electron from the halide. An investigation of different halides (iodide and bromide) enables the construction of a more generalized picture for the structural dynamics involved in solvation processes.

2 Optical transient absorption

Preceding the investigation of CTTS excitation in aqueous halides with the structurally sensitive TR-XSS method, the dependencies of the electronic dynamics following on 1-photon or 2-photon excitation of iodide with different amounts of excess excitation energy were also studied. The absorption spectrum of aqueous NaI in the deep UV exhibits well defined absorption bands centered at 195 nm and 225 nm. These bands shown in Fig. 1a) have been established[50,51] to arise from excitation to spin–orbit split 6s Rydberg-like states, $^2P_{3/2}$ and $^2P_{1/2}$, as schematically drawn in Fig. 1b).

In the present study, optical transient absorption measurements were performed with 1-photon, 240 nm (0.5 μJ per pulse), and 2-photon, 387 nm (20 μJ per pulse), pump pulses on iodide solutions (25 mM) prepared from the sodium salt. A full description of the experimental details is given in the ESI

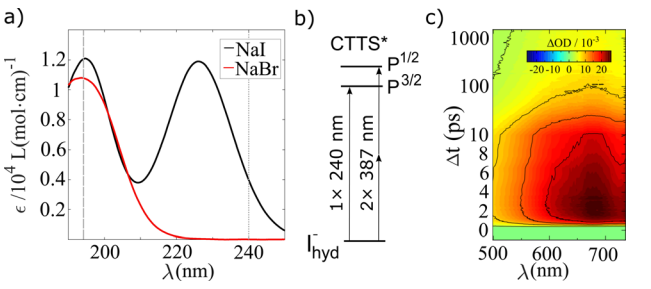

Fig. 1 (a) Static absorption spectra for NaI and NaBr solvated in water. The dashed and dotted grey lines indicate the excitation wavelengths that were used for TA spectroscopy. (b) Scheme of the iodide excitation with 1-photon (240 nm) and 2-photons (387 nm). (c) Transient optical absorption spectrum of aqueous iodide after 240 nm excitation.

Section A.† By performing TA experiments at 240 nm, the 1-photon process at the red tail of the spectrum produces an abstracted electron with a minimal amount of excess energy, while the 2-photon pump excites the system more resonantly into its CTTS state. Thus, the electrons produced with a 2-photon pump have more excess energy. Fig. 1c) shows transient absorption spectra $\Delta A(\lambda, \Delta t)$ of aqueous NaI after 1-photon excitation. Similar to previous spectroscopic studies of solvated electron systems,[37,52,53] the data exhibits the absorption peak centered at ~680 nm[54,55] with a FWHM of 300 nm. The signal increases on a sub-ps time scale and maximum peak height is observed at a time delay $\Delta t = 2.5$ ps and decays on a time scale of tens of picoseconds.

The transient absorption signal was fitted in a global analysis framework including three components, with one describing the grow-in of the signal and two describing the decay yielding as output three time constants τ_1, τ_2, and τ_3. For the 1-photon excitation of NaI, this analysis yields a characteristic grow-in time of $\tau_1 \approx 400$ fs, followed by a fast decay of about 60% of the signal on a time scale of $\tau_2 \sim 19$ ps with the remaining signal decaying on a time scale of a few hundred ps. Similar time constants are observed for 2-photon excitation, although only 30% of the signal decays with the fast time component in the 2-photon case. The best-fit parameters and results are summarized in Table 1 and Fig. S1–S2 in the ESI.†

3 Time-resolved X-ray solution scattering

TR-XSS data were collected at both the ID09 beamline[56] at the European Synchrotron Radiation Facility (ESRF) at pump – probe time delays of $\Delta t = 200$ ps to several nanoseconds and at the SACLA X-ray free electron laser for pump-probe time delays $\Delta t = -20$ ps to 100 ps. Aqueous iodide and bromide were studied at two different concentrations, 20 mM and 100 mM, respectively.

At ESRF, a 300 μm flat liquid jet with a NaI sample was 2-photon excited with 50 fs laser pulses at 400 nm wavelength on a spot size of 160 × 140 μm and a pulse intensity of 73 μJ per pulse at the sample position. The 18 keV X-ray probe pulses (100 ps pulse width) were generated in a 1 kHz mode using a high speed chopper system.[57] Scattering signals $S(Q)$ were recorded with a Rayonix detector as a function of the wave vector transfer $Q = \frac{\lambda}{4\pi}\sin(\theta)$, where 2θ is the scattering angle and λ the X-ray wavelength.

At SACLA, the aqueous iodide and bromide samples were delivered to the beam interaction point as a 50 μm round jet and two sets of experiments were performed; in one, the samples were excited with ~50 fs laser pulses at 202 nm wavelength produced with the fourth harmonic of the Ti:sapphire laser for 1-photon excitation. The spot size was 150 × 170 μm with a laser flux of 8 μJ per pulse at the sample position. In a second set of experiments at SACLA, pump pulses of 400 nm wavelength were used for 2-photon excitation with a spot size of 250 × 260 μm and with an intensity of 70 μJ per pulse. 15 keV X-ray probe pulses were delivered with 30 Hz repetition rate and a pulse length below 10 fs. The time delay between the laser-pump and the X-ray probe pulses was determined with better than 50 fs accuracy on a pulse-to-pulse basis utilizing the arrival time monitor instrument installed immediately before the sample chamber.

In both the synchrotron and the X-ray free-electron laser experiment, the 2-dimensional detector data was reduced by azimuthal integration around the center of the detector ($\theta = 0$). Subsequently, difference scattering curves were obtained through the subtraction of laser-off from the laser-on scattering curves, as indicated in eqn (1). Further information on data reduction and the signal scaling to the smallest stoichiometrically representative unit of the solution (Liquid Unit Cell, LUC) can be found in the ESI.†

$$\Delta S(Q, \Delta t) = S_{on}(Q, \Delta t) - S_{off}(Q) \quad (1)$$

The high temporal resolution available at SACLA enables studies of sub-picosecond structural dynamics following photoabstraction excitation of I^- and Br^- in aqueous solution. Fig. 2a–c shows 2-dimensional representations of the recorded $\Delta S(Q, \Delta t)$ difference signals for aqueous NaI, aqueous NaBr and pure water excited with 202 nm pump pulses at a similar incident laser fluence. In all three measurements, the strongest difference signal is a positive feature surrounded by two negative signal features and is observed between $Q = 1.5$–4 Å^{-1}. This

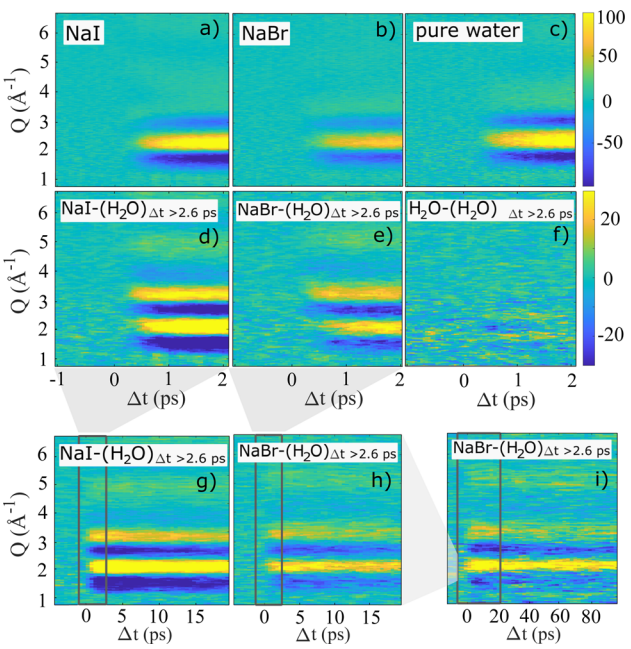

Fig. 2 2-dimensional representations of $\Delta S(Q, \Delta t)$ after excitation with 8 μJ 202 nm pump pulses. In (a)–(c) the full signal is shown for aqueous NaI, aqueous NaBr (both 100 mM) and pure water for time delays up to 2 ps. In (d)–(i) an averaged pure water signal for $\Delta t \geq 2.6$ ps was fitted to and subtracted from the full signal. The three bottom panels show data at longer time delays up to (g), (h) $\Delta t = 20$ ps and (i) $\Delta t = 100$ ps. The area of the zoom-in of the preceding panels is marked by a grey box.

pattern is consistent with the TR-XSS signature arising from the structural changes due to a temperature increase of the aqueous solvent.

Fig. 2d–i demonstrates how a time-dependent subtraction of the neat water heating difference signal obtained at $\Delta t > 2.6$ ps reveals the presence of a significantly weaker (note the change in color scale) but persistent difference signal in the data sets acquired for NaI and NaBr, but not for neat water. Thus, panels d–i show solely the difference scattering arising from electron-abstraction from the halides and the subsequent structural dynamics, with panels d and e focusing on the fastest time scales ($\Delta t < 2$ ps), g and h the intermediate time scale up to 20 ps and panel i shows the heat-subtracted difference signal for NaBr up to $\Delta t = 100$ ps. For panels g–i the dark rectangles indicate the time range shown in the previous panels. For both NaI and NaBr the heat-subtrated difference signal is observed to appear on a sub-picosecond time scale and are quite similar in shape for the two halides. For both systems the difference signal is observed to decrease in intensity on a time scale of tens of picoseconds with no change in difference signal shape but with significant difference signal intensity also remaining out to the longest time delays studied at SACLA. The difference scattering $\Delta S(Q, \Delta t)$ obtained from aqueous NaI after 2-photon excitation with 400 nm pump pulses does not display any distinctive changes in difference signal shape or time evolution compared to the 1-photon process and is shown in the ESI.†

3.1 Modeling the difference scattering

The scattering from each of the subsystems (solute, cage and bulk solvent) can be calculated from the pairwise radial distribution functions $g_{lm}(r)$ between atoms of 'type' (*i.e.* atomic form factor[58]) l and m *via* the generalized form of the Debye equation

$$S(Q) = \sum_l N_l f_l^2 + \sum_{l,m} f_l f_m \frac{N_l(N_m - \delta_{lm})}{V} 4\pi \times \int_0^\infty r^2 g_{lm}(r) \frac{\sin(Qr)}{Qr} \mathrm{d}r, \quad (2)$$

where N_l denotes the number of atoms of type l, f indicates atomic form factors (with the dependence on Q suppressed for clarity of presentation), r is the distance between atoms, V is the irradiated volume, and δ_{lm} is the Kronecker delta. The radial distribution functions (RDFs) that describes the sample can be modelled by performing Molecular Dynamics (MD) simulations and histogramming the interatomic distances from the simulation. The specifics on how to apply eqn (2) to radial distribution functions sampled from MD simulations can be found elsewhere,[59,60] and is summarized for this work in the ESI.†

To interpret the acquired TR-XSS data and assign physical meaning to the shape and evolution of difference scattering signals, we utilize a model based on a linear combination of difference scattering components arising primarily from the solute, solvation cage and bulk solvent regions of the molecular system, an approach also utilized in previous works.[14,44,61] As in the recent work on iodide solvation dynamics by Vester *et al.*,[44] classical MD simulations are taken as the starting point for calculating the contributions to the (difference) scattering signal arising from structural changes in the solute, the bulk solvent and the solvation cage surrounding the solute species.

MD simulations were performed for charged halides and neutral halogens solvated in water, representing the state of the molecular system before and some time after laser excitation and electron abstraction when structural equilibrium around the halogen solute has been established. Specifically for the cage contribution $S_c(Q)$, the radial distribution function g_{lm} between the halide and oxygen (here I–O) as well as iodide and hydrogen (I–H) atoms is calculated for all such atom pairs. For the solvent the scattering is calculated from the radial distribution function of O–O, O–H and H–H, and is here denoted $S_v(Q)$. In a second calculation step, the difference signal $\Delta S(Q)$ for each of the three contributions is calculated from direct subtraction $\Delta S(Q) = S_{\mathrm{Excited}}(Q) - S_{\mathrm{Ground}}(Q)$ to yield ΔS_u, ΔS_c and ΔS_v, where the latter may include changes in scattering arising from changes in excluded volume while spurious contributions to the simulated difference signal from changes in the density due to the simulation methods have been removed as described in the ESI in Fig. S10 and eqn (7).†

Additionally to the changes in scattering arising from changes in the solute, solvent and shell structures as a consequence of the change in electronic state of the solute, the "heat response" difference signal component $\Delta S_{\Delta T}(Q)$ arising from the structural changes due to energy deposition into the solvent is included. This contribution was measured in a separate experiment.[62] Thus, our full model becomes a linear combination with the following terms:

$$\Delta S(Q, \Delta t) = \alpha(\Delta t) \cdot \Delta S_{u+c}(Q) + \gamma(\Delta t) \cdot \Delta S_v(Q) + \Delta T(\Delta t) \cdot \Delta S_{\Delta T}(Q). \quad (3)$$

In this expression, α can be readily interpreted as an excitation fraction, whereas γ represents both local (near the solute) and bulk changes to the structure of the solvent. As the volume of the solute and solvation shell is inaccessible to the bulk solvent, it has in the past been described as 'excluded volume'. Upon extraction of an electron from the solute the solvation shell first grows and then later, following recombination, shrinks due to reordering around the solvated ion. With the scaling to a LUC, ΔT describes the magnitude of a structural change directly arising from a temperature increase in degrees K when thermodynamic equilibrium has been established as discussed in the ESI† and following the considerations presented in ref. 14.

In the first step of the data analysis presented here, the sensitivity of $\Delta S_{u+c}(Q)$ towards details of the molecular–level interactions is benchmarked for the case of aqueous iodide on picosecond-resolved scattering data measured at the ESRF as follows. In the MD simulations we assume[63–65] that the potential of the solute atoms with respect to the solvent molecules at a particular distance r_{ij} can be described by a Lennard-Jones potential for a pair of atoms i and j

$$V_{ij}(r_{ij}) = 4\varepsilon_{ij}\left[\left(\frac{\sigma_{ij}}{r_{ij}}\right)^{12} - \left(\frac{\sigma_{ij}}{r_{ij}}\right)^{6}\right] \quad (4)$$

with parameters σ_{ij} and ε_{ij} corresponding to the characteristic distances and strengths of the van der Waals interactions. Further, the full potential of iodide I^- towards interaction with the (polar) molecules of the aqueous solvent differs strongly from the iodine (I^0) potential due to the coulombic contribution to the interaction between the charged solute and polar solvent molecules. While many studies[66–70] have been directed towards determining the correct Lennard-Jones (LJ) parameters for the case of iodide, only few[71] of them attempted to determine LJ parameters representing interaction with iodine. Fig. 3a shows total non-bonded pair interaction potentials with water for the charged iodide species (black curve) as well as for two sets of LJ parameters for the non-charged iodine species (see the ESI† for details). The grey line depicts the LJ potential when the same parameters are used for iodine as for iodide (σ = 5.02 Å, ε = 3.7 kJ mol^{-1}) and the green line shows the LJ potential where the parameter set σ = 3.75 Å, ε = 2.51 kJ mol^{-1} is used for iodine, which is derived from an optimization of the free energy of hydration for alkyl halides in a TIP4P water model.[71] The potential for the I^- interaction shows a clear and deep minimum at R = 3.9 Å, with the gray curve resulting from using the same LJ parameters for I^- and I^0 having a much more shallow minimum at a longer distance, around 4.6 Å, due to the absence of the electrostatic interaction. The green potential energy curve calculated using the I^0-optimized LJ parameters shows a similarly shallow minimum, but at a shorter distance of about R = 3.9 Å.

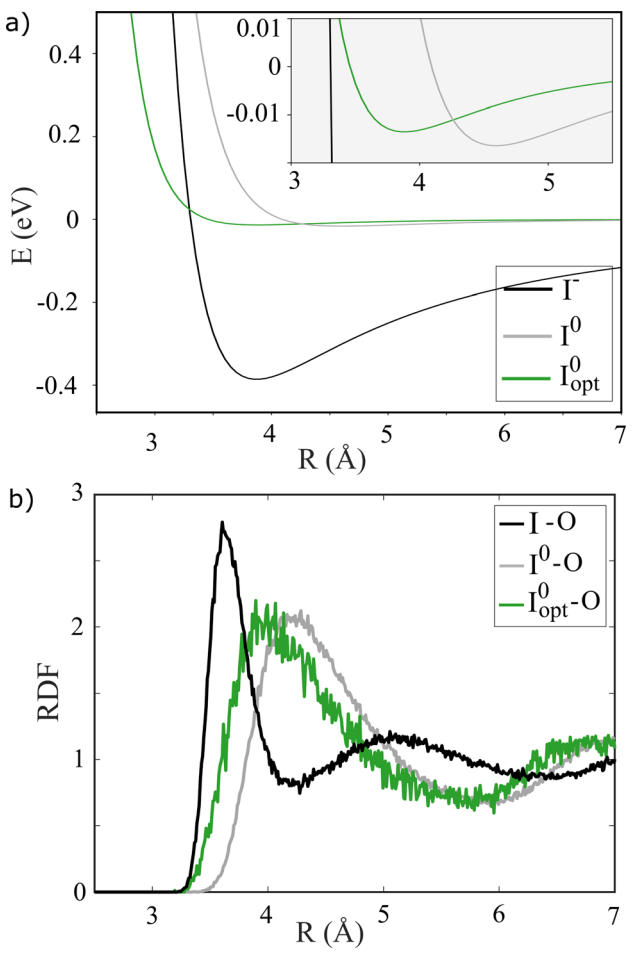

Fig. 3 (a) Iodide/dine-water dimer potential curves based on the dimer geometry determined in Fig. S3 in the ESI,† calculated using iodide and the excited state iodine with (I_{opt}^0) and without (I^0) optimized parameters. (b) RDFs calculated by classical MD simulation for the halide-oxygen distance of aqueous NaI.

Fig. 3b shows the structural consequences of these three different interaction potentials in terms of the I–O radial distribution functions calculated from MD simulations. The strong interaction between solute and solvent in the I^- case (black curve) leads to a very well-defined first solvation shell with an I–O distance of about 3.6 Å as well as clear signatures of also well-defined 2nd shell at 5 Å. For the case of I^0, the first solvation shell is less well defined and is found at longer I–O distances, 4–4.5 Å, and also here a 2nd solvation shell can be discerned at a distance of 7 Å. While the resulting solvation structures are generally quite similar for the two sets of LJ parameters used for I^0, the assumption of the same LJ interaction parameters for I^- and I^0 (grey curve) leads to a slightly longer 1st shell distances than the simulation based on LJ parameters optimized from alkyl halide simulations. As discussed in further detail below, it is interesting to note how even rather different solute–solvent interaction potentials lead to essentially the same solvation shell structures in the case of I^0, indicating that solvent–solvent interactions may dominate over solute–solvent interactions for this species.

To demonstrate how the TR-XSS methods employed in the present study have the needed sensitivity to discern between different models for the solute–solvent interactions for I^0, Fig. 4a) shows the ΔS_{u+c} term calculated from the two I^0 MD simulations. Even though the two ΔS_{u+c} curves are quite similar, employing the LJ parameters optimized for I^0 leads to a significantly (χ^2 = 2.2 *vs.* χ^2 = 3.1) better fit to the X-ray difference scattering signal $\Delta S(Q)$ acquired at Δt = 200 ps, compared to using the same LJ parameters for I^0 as for I^-. Fig. 4b shows the full fit as well as the individual contributions to the model for the $I^- \rightarrow I^0$ photo-abstraction difference scattering signal.

In the following Section, ΔS_{u+c} is calculated with the optimized LJ parameters and the same linear-combination analysis approach is applied to follow the dynamics of solvation immediately following photo-abstraction of the electron from I^-. We note, that for clarity in Fig. 4b the signal contributions from direct water excitation and photoproduct formation have been removed from the difference signal ΔS, which leaves ΔS_{u+c} as the strongest signal contribution.

3.2 Time-dependence of the scattering signal contributions

To investigate the time evolution of the acquired difference signals in more detail, we next apply the model presented in eqn (3) to fit the data shown in Fig. 2a and b. Fig. 5 shows the (heat-subtracted) $\Delta S(Q, \Delta t)$ data for the NaI sample as well as the model fit and the residual. Corresponding fit results for longer time delays, lower concentration and for NaBr are shown in the ESI Fig. S6–S9.† In general a very good fit is observed at all time delays with all the major features of $\Delta S_{meas.}(Q, \Delta t)$ being

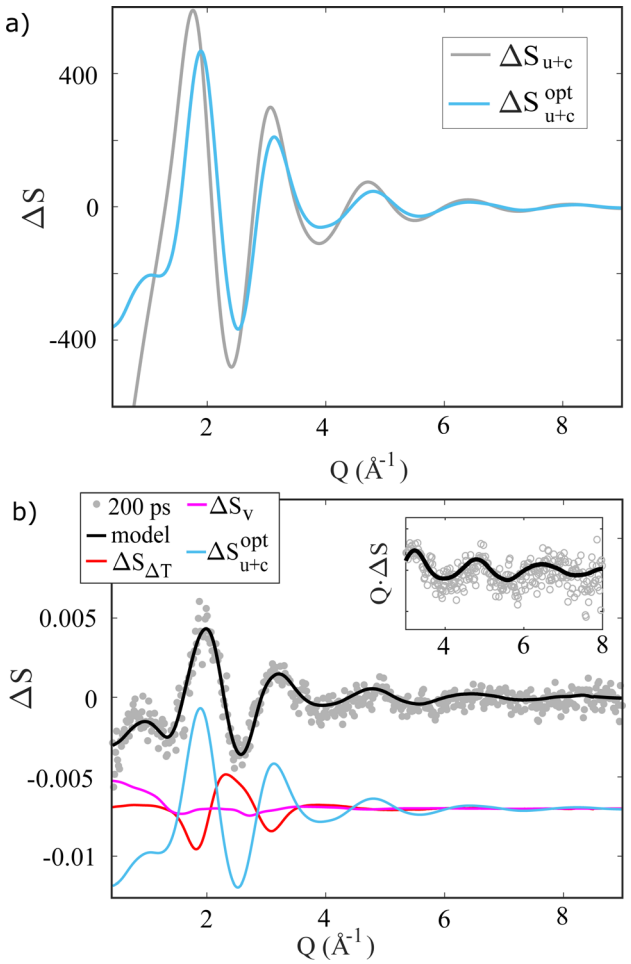

Fig. 4 (a) Difference scattering signals calculated from the RDFs in Fig. 3 *via* the Debye equation. (b) $\Delta S(Q, \Delta t = 200\ \text{ps})$ (water-subtracted, di-/triiodide-subtracted see ESI†) fitted with the scattering contributions, which are shown with an offset for clarity. The inset shows $Q\Delta S(Q, \Delta t)$ in the high Q range.

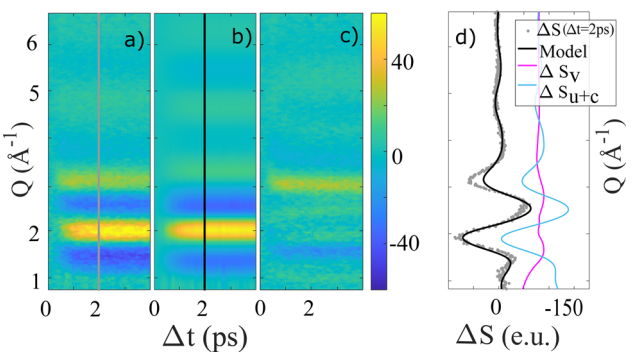

Fig. 5 (a) 2-dimensional representations $\Delta S(Q, \Delta t)$ of the 100 mM NaI measurement (heat-subtracted), (b) the model after eqn (3) and (c) the residual after subtraction the model from the measurement. The lines through $\Delta t = 2$ ps indicate the location for the difference scattering in Q shown in (d).

captured by $\Delta S_{\text{model}}(Q, \Delta t)$, albeit with a tendency for the measured data to show slightly sharper features than what is predicted by the model.

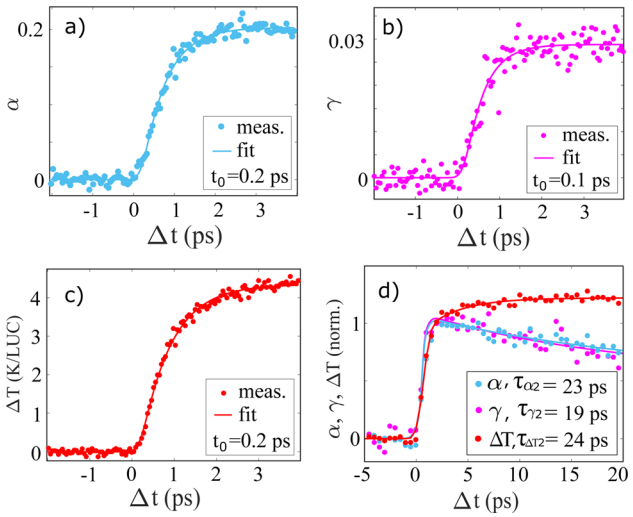

Fig. 6 (a)–(c) Temporal evolution of the three model contributions $\alpha(\Delta t)$ (magenta), $\gamma(\Delta t)$ (cyan) and $\Delta T(\Delta t)$ (red) for 100 mM aqueous NaI after 202 nm excitation. Full lines are fits of IRF-broadened exponential grow-ins with the best-fit time constants indicated in the legends. (d) Long time delay behaviours of $\alpha(\Delta t)$, $\gamma(\Delta t)$ and $\Delta T(\Delta t)$. The solid lines show best-fit exponential decays (for α, γ) and grow-in (for ΔT) with the time constants τ indicated in the legend.

Fig. 6a–c shows the time evolution of the three time-dependent scalers in the model described by eqn (3). $\alpha(\Delta t)$ and $\gamma(\Delta t)$ and $\Delta T(\Delta t)$ all show very similar behavior, with a grow-in completed on the ~1 ps time scale. To quantify these dynamics further, Fig. 6 also shows the best-fit results for an exponential grow-in (broadened by an Instrument Response Function (IRF) as shown in eqn (E8)–E10†) fitted individually to each of $\alpha(\Delta t)$ and $\gamma(\Delta t)$ and $\Delta T(\Delta t)$ in the time range up to 4 picoseconds. To stabilize the fitting the width of the IRF was constrained to a 120–140 femtoseconds interval, but inspired by the delayed-onset observed in the previous study by Vester *et al.*,[44] the time of the onset (t_0) was included as a fully free parameter.

From these fits, we find that for the 100 mM NaI sample $\alpha(\Delta t)$ and $\gamma(\Delta t)$ show a delayed onset of 0.1–0.2 ps with respect to $\Delta t = 0$, in agreement with the results presented in Vester *et al.* For the time scale of the signal grow-ins we find that the ΔS_v contribution grows in slightly faster ($\tau_\gamma = 0.4(1)$ ps) than the ΔS_{u+c} contribution ($\tau_\alpha = 0.6(1)$ ps). Although at the limit of resolvability we find this trend to be reproduced across the four sample types investigated, as shown in Table 1.

Table 1 Comparison between rise times of $\alpha(\Delta t)$, $\gamma(\Delta t)$ and $\Delta T(\Delta t)$ after 1-photon excitation, the decay times $\alpha 2(\Delta t)$, $\gamma 2(\Delta t)$ and the second rise time $\Delta T2(\Delta t)$ in picoseconds

Sample	τ_α	τ_γ	$\tau_{\Delta T}$	$\tau_{\alpha 2}$	$\tau_{\gamma 2}$	$\tau_{\Delta T2}$
NaI						
20 mM	0.7(1)	0.6(2)	0.8(1)	21(16)	15(11)	29(32)
100 mM	0.6(1)	0.4(1)	0.7(1)	23(3)	19(6)	24(21)
NaBr						
20 mM	0.7(1)	0.6(1)	0.8(1)	83(120)	15(13)	27(10)
100 mM	0.7(1)	0.6(1)	0.8(1)	18(11)	13(6)	32(13)

$\Delta S_{\Delta T}$ is observed to grow in on a time scale of $\tau_{\Delta T} = 0.7(1)$ ps which is slightly slower than in previously publications,[14,44] which we ascribe to how the model is applied to fit the data here without including the second, slower, grow-in for the $\Delta S_{\Delta T}$ contribution, seen in Fig. 6d) and which is discussed in more detail below. We further note that we do not see the early onset of the $\Delta S_{\Delta T}$ contribution which was observed in the work by Vester *et al.*, and tentatively assign this observation to the much lower laser fluence used in the experiments for which results are presented here.

Generalizing the fit results for 100 mM NaI to the other sample types studied, the first three columns of Table 1 show the time constants τ_α, τ_γ and $\tau_{\Delta T}$ determined from the same analysis applied to similar data sets acquired for 20 mM and 100 mM samples of NaI and NaBr. For all samples, the response of ΔS_v is the fastest ($\tau_\gamma = 0.4$–0.6 ps) followed by ΔS_{u+c} ($\tau_\alpha = 0.6$–0.7 ps) and $\Delta S_{\Delta T}$ ($\tau_{\Delta T} = 0.7$–0.8 ps).

Fig. 6d shows the time evolution of $\alpha(\Delta t)$, $\gamma(\Delta t)$ and $\Delta T(\Delta t)$ on the 20 ps time scale, with Fig. S14 and S15 of the ESI† showing the corresponding data sets acquired for NaBr. For the 100 mM NaI and NaBr samples we find that the ΔS_{u+c} and ΔS_v contributions to the difference signal show a ∼20% decrease on the 20 ps time scale and applying a simple mono-exponential fit to these observed dynamics we find characteristic time constants of around ≈20 ps. For the corresponding 20 mM data the measured difference signals are much weaker and these time constants have a high uncertainty as seen in Table 1. We also note, that the decays do not complete on the 100 ps time scale (see also Fig. S15†), therefore the complete return to an unexcited system has a time scale $\tau_{long} > 100$ ps larger then the probed time range. For the evolution of ΔT Fig. 6d shows how the initial fast grow-in is followed by a second, slower and much smaller, increase in the solvent temperature. From the decay of $\alpha(\Delta t)$ an estimation of an average electron ejection radii of $r_{ej} = 5.3 \pm 3$ Å for iodide and $r_{ej} = 7.5 \pm 4$ Å for bromide is calculated based on the diffusion-limited recombination model discussed by Vester *et al.*[44] The distributions of r_{ej} are shown in the Fig. S17.†

To investigate the signal dependence on single- or multi-photon excitation on short time scales, Fig. 7 shows $\Delta S(Q, \Delta t = 2\text{ ps})_{NaI} - \Delta T \cdot \Delta S_{H_2O}$ after 1-photon excitation at 202 nm and 2-photon excitation at 400 nm. Both wavelengths excite aqueous iodide into the CTTS band centered at 195 nm. For 2-photon excitation, the lower signal to noise ratio is a consequence of the smaller excitation fraction for the multi-photon process. The shape of the depicted signal as well as the similar grow-in show no excitation-dependent changes within the measurement uncertainties.

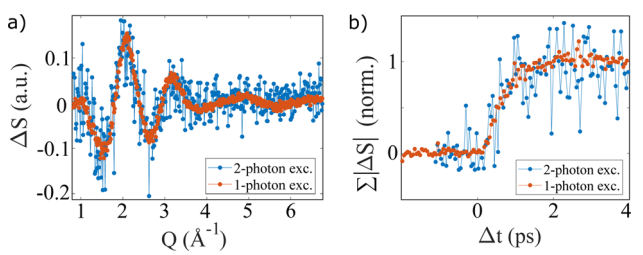

Fig. 7 Comparison between 1-photon and 2-photon excitation of 100 mM NaI. Panel (a) depicts $\Delta S(Q, \Delta t = 2$ ps) after subtracting contributions from pure water scattering and in (b) the sum of the absolute signal is shown as a function of Δt up to 4 ps.

4 Discussion

4.1 Transient optical absorption data

In the TA measurement results shown in Fig. 1c the signature of a solvated electron is to be observed with a grow-in time $\tau_1 \sim 400$ fs for CTTS excited iodide in water. Based on the time-independent position of the absorption peak, a low probability for the formation of cation–electron pairs[53,72–74] in the solution can be assumed. The signal decay is bi-exponential (τ_2, τ_3), where the signal dies out after a characteristic time τ_3 in accordance with earlier studies,[37,40] matching a diffusion driven recombination of free electrons with the halogen atoms. As the observed lifetimes τ_2 are too short for free diffusion through the solvent, we cautiously ascribe them to the geminate recombination of electrons in close proximity of their original halogen atom. Such electrons match the description of short-lived contact-pairs by Staib and Borgis.[25] The number of electrons staying in close proximity gets smaller when the (average) ejection distances grow larger. With the amplitudes $\frac{a_2}{a_{total}}$ we tentatively approximate the number of contact-pair-like electrons to 60% at 240 nm excitation and 30% at 387 nm excitation.

4.2 Solvation structure of I^0

Turning next to the analysis and interpretation of the TR-XSS data, Fig. 4b demonstrates how the comparatively simple model presented in eqn (3) is able to fully capture all features of the background-subtracted difference scattering signal acquired at $\Delta t = 200$ ps after 2 × 400 nm photoexcitation. As indicated by the light blue curve in this figure, after water-subtraction $\Delta S(Q)$ is dominated by the difference signal contribution ΔS_{u+c} arising from changes in the solute–solvent pair-correlation function due to photo-abstraction of an electron from I^-, but with some contribution from the changes in the solvent–solvent radial distribution function which give rise to ΔS_v. This latter contribution can tentatively be related to the change in the size of the "hole" in the solvent occupied by the solute (excluded volume) as well as potentially to the changes in inter-molecular structure arising from the several millimolar of solvated electrons e_{aq}.[52,75–77]

The dominating ΔS_{u+c} contribution arises from the structural changes seen from the "point of view" of the solute and as such is directly related to the structural changes in the first solvation shell(s) which are illustrated by the $g(r)$'s in Fig. 3b). As discussed in the Introduction, these structural changes have been robustly demonstrated to consist of a ∼0.5 Å expansion and broardening of the well-defined solvation shell determined for I^-.[43,44,67–71] The well-defined solvation structure of aqueous I^- arises primarily due to the strong electrostatic interactions

between the charged halide species and the polar water molecules and has been characterized experimentally in many studies.[32–42,44] This has allowed a good description of the I^-–H_2O interaction potential(s) from theory, but much fewer studies exist for I^0 (ref. 63) and there is thus currently no consensus about the shape of the I^0–H_2O interaction potential. As demonstrated in Fig. 3b and 4a, MD studies show how changes to this interaction (parameterized *via* the LJ parameters) lead to subtle yet distinctive changes in $g(r)$ as well as in the ΔS_{u+c} calculated therefrom. This allows a benchmark of two sets of putative LJ-parameters against the acquired TR-XSS data, and we find that an I^0–H_2O interaction potential described by $I_{opt}{}^0$ LJ parameters of $\sigma = 3.75$ Å^{-1} and $\varepsilon = 2.51$ kJ mol^{-1} derived from optimization against alkyl halides and halobenzenes by Jorgensen *et al.*[71] give a significantly better fit to the data compared to using the same I^- LJ-parameters for also I^0. A more detailed investigation of the halogen–water interaction for the neutral atomic species I^0 and Br^0 using TR-XSS will be reported elsewhere.

4.3 Structural dynamics

Having established the applicability of the model represented in eqn (3) on the well studied system iodide, we next move to the interpretation and discussion of the femtosecond-resolved results presented in Fig. 2 and 5–7. The results shown for iodide and the smaller bromide species are similar, which has hitherto not been investigated with time-resolved X-ray methods. As evident from Fig. 2a–c, 202 nm photo-excitation of 100 mM aqueous NaI, NaBr as well as neat H_2O leads to the appearance of clear difference scattering signal. The difference signal obtained for neat H_2O very closely resembles the well-known difference scattering signal arising from isobaric heating of water as shown in Fig. S20.† As discussed in the original work by Quickenden & Irvin[78] the absorption coefficient of even ultrapure water at 202 nm while very low, is not zero and the presence of impurities or dissolved O_2 may increase the absorption by an order of magnitude or more. Given the linear, no-threshold behaviour of the magnitude of the difference signal measured for neat water as a function of incident laser fluence we ascribe the presence of this "background" contribution of $\Delta S(Q, \Delta t)$ primarily to a consequence of 1-photon absorption by the water molecules or impurities such as dissolved O_2 which we did not take any precautions to remove beyond using milliQ water. However, as Fig. 2d–f shows, this contribution to $\Delta S(Q, \Delta t)$ from direct heating of water can be subtracted as $\Delta S_{Meas}(Q, \Delta t) = \Delta S_{Full}(Q, \Delta t) - \Delta S_{H_2O,\Delta t>2.6ps}(Q, \Delta t)$ revealing distinct difference scattering signals in the NaI and NaBr data sets and essentially no residual for neat water.

Fig. 5 illustrates how the heat-subtracted difference signal from NaI is very well captured on the single-picosecond time scale by the comparatively simple model presented in eqn (3) and benchmarked against the $\Delta t = 200$ ps data. From inspection of the residual between data and model in Fig. 5, the measured difference signal shows slightly sharper features than the one modelled, indicating that (changes in) the actual structural motifs giving rise the ΔS_{u+c} may be more well-defined compared to the model results shown in Fig. 4. Furthermore, the absence of any significant time evolution in the shape of the residual (see ESI Fig. S9†) supports the use of difference signals calculated from equilibrium simulations for I^- and I^0 to model the dynamics following photo-abstraction. This in turn indicates that this model component changes only in magnitude and not in signal shape as a function of time.

Fitting eqn (3) to the difference signal $\Delta S(Q, \Delta t)$ for NaI allows us to determine the evolution of the three individual components of the difference signal as Fig. 6 shows. For all three components we observe that there is a short offset ($t_0 =$ 0.1–0.2 ps) between the arrival time of the 202 nm excitation pulse and the onset of the structural dynamics. As X-ray scattering is much more sensitive to the more electron-rich oxygen atoms relative to the hydrogen atoms, this short "wait time" can be related to the time scale of break-up of the hydrogen-bond network which in turn allows the oxygen atoms to move.[44]

Following the short wait time (t_0) the ΔS_v as well as the ΔS_{u+c} contributions increase in magnitude with time constants $\tau_\alpha =$ 0.6–0.7 ps and $\tau_\gamma =$ 0.4–0.6 ps, reaching their full magnitudes after about a picosecond. Returning to eqn (3) and how ΔS_{u+c} and ΔS_v are defined and simulated, we therefore conclude that the structural changes described in Fig. 3 (expansion of the first shell) are completed on this time scale. How this concept also applies to multiple photon excitation is shown in Fig. 7, where we conclude that electron-abstraction from a single halide ion in water is a similar process after 1- or 2-photon excitation with the same total energy. As seen in Fig. 3a, the driving force for this structural re-arrangement can be directly understood as a consequence of a vertical excitation from the I^-–O potential surface (black line) to one of the I^0–O potential surfaces (green and grey). The driving force $F = -\frac{dU}{dr}$ ensues the potential and is dependent on where and on which potential energy surface the system finds itself after photoabstraction. As such not only the shape of the difference signal (Fig. 4a) but also the dynamics may be a sensitive probe of the I^0–O interaction potential. Further future structural studies could also be targeted towards the (possibly transient) existence of the I–OH_2 pairs not seen in our classical MD simulations but observed in previous *ab initio* MD simulation studies.[35,43]

4.4 Recombination dynamics

As described in the section on TR-XSS, the $\alpha(\Delta t)$ parameter on time scales where the structural dynamics have been completed has a direct interpretation as an excitation fraction, *i.e.* how large a fraction of the initial I^- population is in the charge-neutral I^0 state at time Δt. Fig. 6d shows the evolution of $\alpha(\Delta t)$ as well as $\gamma(\Delta t)$ and $\Delta T(\Delta t)$ on the 20 ps time scale, and a clear decrease in the excitation fraction is observed. This is shown for longer time scales in the ESI Fig. S13† from which it is evident that the excitation fraction does not follow a mono-exponential decrease towards 0 but reaches a plateau at α_{long}. Further, on the same time scale as we observe the fraction of I^0 decrease, we find an increase in solvent temperature, ΔT, which we associate with the energy released upon $e_{aq} + I^0 \rightarrow I^-$ recombination.

The primary observable in the present X-ray scattering study is the change in distance between the iodide and the oxygen atoms of the surrounding water molecules, therefore, the details of the electron localization process in the bulk solvent are at present very hard to track or quantify, as no X-ray scattering signatures of the neither delocalized nor localized electron have yet been published. High resolution TR-XAS might shed further light on the orbital character as well as the delocalization and localization dynamics of the electron in the future. For now, we concentrate on interpreting the observation of a two-step decay in the fraction of the I^0 species as arising from the photo-abstracted electrons being ejected at $\Delta t = 0$ to form a population of photo-ejected electrons with a mean distance r_0^{ej} from the parent halide, in line with the analysis presented in previous work.[44] This population subsequently evolves in time with some fraction diffusing in the general direction of the parent halide and some towards the bulk solvent. This leads to two time scales for $e_{aq} + I^0 \rightarrow I^-$ recombination, with the faster one ($\tau_2 = 19$ ps in the TA experiment, $\tau_{\alpha 2} \approx 20$ ps in the TR-XSS experiment) representing the so-called primary geminate recombination for the fraction of the photo-ejected electron population diffusing initially towards the parent halide. The second time scale (>100 ps) characterizes the secondary geminate recombination where the electron initially diffuses towards the bulk before eventually recombining with the parent halide, with potentially a third time scale (which depends on excitation fraction and initial halide concentration) representing non-geminate recombination with other neutral halogens having undergone photoabstraction. The fraction and time scale of primary geminate recombination depends on the details of the $e_{aq} + I^0$ interaction potential in the presence of water but in line with the conclusions of the recent work presented in Vester *et al.*[44] , we here limit our analysis to a minimal assumption of pure diffusion, *i.e.* with a flat $e_{aq} + I^0$ interaction potential, and immediate recombination at a specified distance $r_{rec.}$. Applying this framework (see Fig. S17†) we find that for NaI the reconstructed distribution is centered at $r_0^{ej} = 5$ Å, and extends beyond 10 Å. For NaBr, which from Table 1 exhibits a similar time scale for the primary geminate recombination, the distribution is even broader, and has a maximum at $r_0^{ej} = 8$ Å. These values are broadly in agreement with the previous results presented by H. Iglev *et al.*[79] (optical data) and by Vester *et al.*[44] (XANES data), but we note that (in line with the analysis presented in the ESI† of ref. 44) a preliminary sensitivity analysis indicates that r_0^{ej} and the distribution width depends strongly on the parameter choice for the (temperature-dependent) mutual diffusion coefficient D' and the recombination distance $r_{rec.}$. The temperature dependence of D' in particular complicates the picture, as excess energy from the photo-excitation is released to the solvent following electron abstraction and localization, leading to locally "hot" solvent. A full analysis of the presently used model as well as similar approaches and with the halide/halogen species as the key observable would be highly interesting, but is not feasible with the S/N level of the data sets and analysis results presented here.

Summarizing these observations and time scales in relation to previous studies with optical[36,38,79] and photo-electron[39,40] methodologies, then we find that despite the difference in main observable (halogen *vs.* electron) there is good agreement that the jointly established time scale of ~20 ps can be associated with primary geminate recombination. There is, however, significant differences in the underlying modelling, as the optical approaches introduce several intermediate species to account for complicated changes in the measured spectra, whereas we here find that a simpler diffusion-driven model with no structurally well-defined intermediates is able to fully account for the observed dynamics as seen from the solute "point of view".

5 Conclusions

In this work, we have presented results of optical TAS and TR-XSS experiments on aqueous iodide and bromide excited with 202 nm laser pulses which induce photoabstraction, $I^- + h\nu \rightarrow I^0 + e_{aq}$. The optical experiments observe the photoreaction from the point of view of the photoabstracted electrons whereas the X-ray experiments primarily track the structural dynamics as observed from the point of view of the halogen species. We observe good agreement between the time scales observed with the two methods. Structural analysis of the TR-XSS data demonstrated how the method has a level of sensitivity to the details of the structural re-arrangement of the solvation structure that allows benchmarking of parameters describing the solute–solvent interactions. From quantitative analysis of the acquired TR-XSS data we conclude that for both halide species the structural dynamics involve a delay in the signal onset on a 0.1 ps time scale, a delay which we ascribe tot he time scale for an initial breaking of the H-bond network. Following this, we observe an X-ray difference scattering signal which can be assigned to a structural re-arrangement of the nearest solvent molecules taking place on a time scale of about 0.5–1 ps. On longer time scales we observe primary and secondary geminate recombination $e_{aq} + I^0 \rightarrow I^-$ with dynamics that are well captured by simple diffusion of electrons ejected to the solvent as broad distribtuons with mean distances of about 5 Å (NaI) and 8 Å (NaBr). The quality of the TR-XSS data and structural sensitivity analysis indicates significant opportunities for investigating the details and dynamics of the halide/halogen-water interaction potentials in further detail in future works.

Data availability

ESRF data is available at **https://data.esrf.fr/doi/10.15151/ESRF-DC-1554640385**. More data will be available upon reasonable request.

Author contributions

VM: formal analysis, investigation, project administration, visualization, writing; JP: formal analysis, software; BLH: investigation; MLH: investigation; AN: investigation; PL: investigation; ML: resources, software; TK: resources, software; SIA: resources; SGB: investigation; FT: funding acquisition, resources; AOD: investigation, data curation, methodology, software; KBM: conceptualization, methodology; MMN:

methodology; KH: conceptualization, funding acquisition, methodology, project administration, writing. All authors contributed with comments to the final version of the manuscript.

Conflicts of interest

There are no conflicts to declare.

Acknowledgements

VM, JP, BLH, MLH and KH gratefully acknowledge support from the Novo Nordisk Foundation NERD program under Grant No. NNF20OC0061740. KBM. and MMN. thank the Independent Research Fund Denmark for support under Grant No. 802100347B. AOD thanks the Icelandic Research Fund, grant 196279-051. The DTU-affiliated authors gratefully acknowledge DANSCATT for supporting the beamtime efforts. TK acknowledges support from JSPS KAKENHI (grant nos. JP19H05782, JP21H04974 and JP21K18944). TR-XSS measurements were performed at BL3 of SACLA with the approval of the Japan Synchrotron Radiation Research Institute (JASRI, proposal no. 2022A8038). The European Synchrotron Radiation Facility (ESRF) is kindly acknowledged for provision of beamtime at the ID09 beamline. The authors would like to thank Pierre Lloria from the Partnership for Soft Condensed Matter (PSCM) at the ESRF. We thank the Kiel University for generous allocation of time at the Transient Absorption Spectroscopy laboratory. We thank Katharina Kubicek (Hamburg University) for sharing her matlab scripts for electron ejection distance calculations.

Notes and references

1 Y. Marcus, *Chem. Rev.*, 2009, **109**, 1346–1370.
2 M. Maroncelli, *J. Mol. Liq.*, 1993, **57**, 1–37.
3 K. H. Kim, J. H. Lee, J. Kim, S. Nozawa, T. Sato, A. Tomita, K. Ichiyanagi, H. Ki, J. Kim, S.-i. Adachi, *et al.*, *Phys. Rev. Lett.*, 2013, **110**, 165505.
4 K. A. Dill, T. M. Truskett, V. Vlachy and B. Hribar-Lee, *Annu. Rev. Biophys. Biomol. Struct.*, 2005, **34**, 173–199.
5 A. Kumar, D. Becker, A. Adhikary and M. D. Sevilla, *Int. J. Mol. Sci.*, 2019, **20**, 3998.
6 N. Nandi, K. Bhattacharyya and B. Bagchi, *Chem. Rev.*, 2000, **100**, 2013–2046.
7 G. R. Fleming and M. Cho, *Annu. Rev. Phys. Chem.*, 1996, **47**, 109–134.
8 C.-R. Wang, J. Nguyen and Q.-B. Lu, *J. Am. Chem. Soc.*, 2009, **131**, 11320–11322.
9 A. Nimmrich, M. R. Panman, O. Berntsson, E. Biasin, S. Niebling, J. Petersson, M. Hoernke, A. Bjorling, E. Gustavsson, T. B. van Driel, *et al.*, *J. Am. Chem. Soc.*, 2023, **145**, 15754–15765.
10 E. H. Choi, Y. Lee, J. Heo and H. Ihee, *Chem. Sci.*, 2022, **13**, 8457–8490.
11 K. H. Kim, J. G. Kim, S. Nozawa, T. Sato, K. Y. Oang, T. W. Kim, H. Ki, J. Jo, S. Park, C. Song, *et al.*, *Nature*, 2015, **518**, 385–389.
12 A. Rondi, Y. Rodriguez, T. Feurer and A. Cannizzo, *Acc. Chem. Res.*, 2015, **48**, 1432–1440.
13 T. Katayama, T.-K. Choi, D. Khakhulin, A. O. Dohn, C. J. Milne, G. Vankó, Z. Németh, F. Lima, J. Szlachetko, T. Sato, *et al.*, *Chem. Sci.*, 2023, **14**, 2572–2584.
14 K. Haldrup, W. Gawelda, R. Abela, R. Alonso-Mori, U. Bergmann, A. Bordage, M. Cammarata, S. E. Canton, A. O. Dohn, T. B. Van Driel, *et al.*, *J. Phys. Chem. B*, 2016, **120**, 1158–1168.
15 E. Biasin, Z. W. Fox, A. Andersen, K. Ledbetter, K. S. Kjær, R. Alonso-Mori, J. M. Carlstad, M. Chollet, J. D. Gaynor, J. M. Glownia, *et al.*, *Nat. Chem.*, 2021, **13**, 343–349.
16 D. Laage and J. T. Hynes, *Proc. Natl. Acad. Sci. U. S. A.*, 2007, **104**, 11167–11172.
17 M. Reidelbach, M. Bai, M. Schneeberger, M. S. Zollner, K. Kubicek, H. Kirchberg, C. Bressler, M. Thorwart and C. Herrmann, *J. Phys. Chem. B*, 2023, **127**, 1399–1413.
18 H. J. Wörner, C. A. Arrell, N. Banerji, A. Cannizzo, M. Chergui, A. K. Das, P. Hamm, U. Keller, P. M. Kraus, E. Liberatore, *et al.*, *Struct. Dyn.*, 2017, **4**, 061508.
19 M. Chergui, *Struct. Dyn.*, 2016, **3**, 031001.
20 W. Zhang, R. Alonso-Mori, U. Bergmann, C. Bressler, M. Chollet, A. Galler, W. Gawelda, R. G. Hadt, R. W. Hartsock, T. Kroll, *et al.*, *Nature*, 2014, **509**, 345–348.
21 D. Laage, T. Elsaesser and J. T. Hynes, *Chem. Rev.*, 2017, **117**, 10694–10725.
22 T. Nickerson, E. Antonio, D. P. McNally, M. F. Toney, C. Ban and A. Straub, *Chem. Sci.*, 2022, **14**, 751–770.
23 S. Funkner, G. Niehues, D. A. Schmidt, M. Heyden, G. Schwaab, K. M. Callahan, D. J. Tobias and M. Havenith, *J. Am. Chem. Soc.*, 2012, **134**, 1030–1035.
24 P. Jungwirth and D. J. Tobias, *Chem. Rev.*, 2006, **106**, 1259–1281.
25 A. Staib and D. Borgis, *J. Chem. Phys.*, 1996, **104**, 9027–9039.
26 D. Borgis and A. Staib, *J. Chem. Phys.*, 1996, **104**, 4776–4783.
27 W.-S. Sheu and P. J. Rossky, *J. Phys. Chem.*, 1996, **100**, 1295–1302.
28 X. Chen and S. E. Bradforth, *Annu. Rev. Phys. Chem.*, 2008, **59**, 203–231.
29 J. A. Kloepfer, V. H. Vilchiz, V. A. Lenchenkov, X. Chen and S. E. Bradforth, *J. Chem. Phys.*, 2002, **117**, 766–778.
30 S. Raugei and M. L. Klein, *J. Chem. Phys.*, 2002, **116**, 196–202.
31 J. Heuft and E. Meijer, *J. Chem. Phys.*, 2005, **123**, 094506.
32 M. Antalek, E. Pace, B. Hedman, K. O. Hodgson, G. Chillemi, M. Benfatto, R. Sarangi and P. Frank, *J. Chem. Phys.*, 2016, **145**, 044318.
33 F. Messina, O. Bräm, A. Cannizzo and M. Chergui, *Nat. Commun.*, 2013, **4**, 2119.
34 C. G. Elles, I. A. Shkrob, R. A. Crowell, D. A. Arms and E. C. Landahl, *J. Chem. Phys.*, 2008, **128**, 061102.
35 V.-T. Pham, T. J. Penfold, R. M. Van Der Veen, F. Lima, A. El Nahhas, S. L. Johnson, P. Beaud, R. Abela, C. Bressler, I. Tavernelli, *et al.*, *J. Am. Chem. Soc.*, 2011, **133**, 12740–12748.
36 H. Iglev, R. Laenen and A. Laubereau, *Chem. Phys. Lett.*, 2004, **389**, 427–432.
37 H. Iglev and A. Laubereau, *Laser Applications in Life Sciences*, 2010, pp. 201–209.

38 M. K. Fischer, A. Laubereau and H. Iglev, *Phys. Chem. Chem. Phys.*, 2009, **11**, 10939–10944.
39 Y.-I. Yamamoto, Y.-I. Suzuki and T. Suzuki, *J. Phys. Chem. Lett.*, 2023, **14**, 1052–1058.
40 H. Okuyama, Y.-I. Suzuki, S. Karashima and T. Suzuki, *J. Chem. Phys.*, 2016, **145**, 074502.
41 Y.-I. Suzuki, H. Shen, Y. Tang, N. Kurahashi, K. Sekiguchi, T. Mizuno and T. Suzuki, *Chem. Sci.*, 2011, **2**, 1094–1102.
42 A. Lübcke, F. Buchner, N. Heine, I. V. Hertel and T. Schultz, *Phys. Chem. Chem. Phys.*, 2010, **12**, 14629–14634.
43 J. Lan, M. Chergui and A. Pasquarello, *Nat. Commun.*, 2024, **15**, 2544.
44 P. Vester, K. Kubicek, R. Alonso-Mori, T. Assefa, E. Biasin, M. Christensen, A. O. Dohn, T. B. Van Driel, A. Galler, W. Gawelda, *et al.*, *J. Chem. Phys.*, 2022, **157**, 224201.
45 S. E. Canton, K. S. Kjær, G. Vankó, T. B. Van Driel, S.-i. Adachi, A. Bordage, C. Bressler, P. Chabera, M. Christensen, A. O. Dohn, *et al.*, *Nat. Commun.*, 2015, **6**, 6359.
46 K. Hwan Kim, J. Kim, J. Hyuk Lee and H. Ihee, *Struct. Dyn.*, 2014, **1**, 011301.
47 M. Chergui, *J. Chem. Phys.*, 2019, **150**, 070901.
48 J. Jortner and A. Treinin, *Trans. Faraday Soc.*, 1962, **58**, 1503–1510.
49 M. J. Blandamer and M. F. Fox, *Chem. Rev.*, 1970, **70**, 59–93.
50 A. M. Rizzuto, S. Irgen-Gioro, A. Eftekhari-Bafrooei and R. J. Saykally, *J. Phys. Chem. Lett.*, 2016, **7**, 3882–3885.
51 D. Bhattacharyya, H. Mizuno, A. M. Rizzuto, Y. Zhang, R. J. Saykally and S. E. Bradforth, *J. Phys. Chem. Lett.*, 2020, **11**, 1656–1661.
52 S. J. Park, W. A. Narvaez and B. J. Schwartz, *J. Phys. Chem. Lett.*, 2023, **14**, 559–566.
53 W. A. Narvaez, S. J. Park and B. J. Schwartz, *J. Phys. Chem. B*, 2022, **126**, 3748–3757.
54 D. M. Bartels, K. Takahashi, J. A. Cline, T. W. Marin and C. D. Jonah, *J. Phys. Chem. A*, 2005, **109**, 1299–1307.
55 F.-Y. Jou and G. R. Freeman, *J. Phys. Chem.*, 1977, **81**, 909–915.
56 M. Jankowski, V. Belova, Y. Chushkin, F. Zontone, M. Levantino, T. Narayanan, O. Konovalov and A. Pastore, *Nucl. Instrum. Methods Phys. Res. B: Beam Interact. Mater. At.*, 2023, **538**, 164–172.
57 M. Cammarata, L. Eybert, F. Ewald, W. Reichenbach, M. Wulff, P. Anfinrud, F. Schotte, A. Plech, Q. Kong, M. Lorenc, *et al.*, *Rev. Sci. Instrum.*, 2009, **80**, 015101.
58 A. J. C. Wilson and V. Geist, *International Tables for Crystallography. Volume C: Mathematical, Physical and Chemical Tables*, Kluwer Academic Publishers, Dordrecht/Boston/London, (published for the International Union of Crystallography), 1993.
59 A. O. Dohn, E. Biasin, K. Haldrup, M. M. Nielsen, N. E. Henriksen and K. B. Møller, *J. Phys. B: At., Mol. Opt. Phys.*, 2015, **48**, 244010.
60 A. Dohn, V. Markmann, A. Nimmrich, K. Haldrup, K. Møller and M. Nielsen, *J. Chem. Phys.*, 2023, **159**, 124115.
61 K. Haldrup, G. Vankó, W. Gawelda, A. Galler, G. Doumy, A. March, E. Kanter, A. Bordage, A. Dohn, T. B. van Driel, *et al.*, *J. Phys. Chem. A*, 2012, **116**, 9878–9887.
62 K. S. Kjær, T. B. Van Driel, J. Kehres, K. Haldrup, D. Khakhulin, K. Bechgaard, M. Cammarata, M. Wulff, T. J. Sørensen and M. M. Nielsen, *Phys. Chem. Chem. Phys.*, 2013, **15**, 15003–15016.
63 V. Pham, I. Tavernelli, C. Milne, R. van der Veen, P. D'Angelo, C. Bressler and M. Chergui, *Chem. Phys.*, 2010, **371**, 24–29.
64 A. Karmakar and A. Chandra, *J. Phys. Chem. B*, 2015, **119**, 8561–8572.
65 C. D. Wick and S. S. Xantheas, *J. Phys. Chem. B*, 2009, **113**, 4141–4146.
66 P. Li, L. F. Song and K. M. Merz Jr, *J. Chem. Theory Comput.*, 2015, **11**, 1645–1657.
67 I. S. Joung and T. E. Cheatham III, *J. Phys. Chem. B*, 2008, **112**, 9020–9041.
68 G. H. Peslherbe, B. M. Ladanyi and J. T. Hynes, *Chem. Phys.*, 2000, **258**, 201–224.
69 K. P. Jensen and W. L. Jorgensen, *J. Chem. Theory Comput.*, 2006, **2**, 1499–1509.
70 B. A. Bauer and S. Patel, *J. Chem. Phys.*, 2010, **132**, 024713.
71 W. L. Jorgensen, J. P. Ulmschneider and J. Tirado-Rives, *J. Phys. Chem. B*, 2004, **108**, 16264–16270.
72 B. Bockrath and L. M. Dorfman, *J. Phys. Chem.*, 1973, **77**, 1002–1006.
73 S. Koneshan, J. C. Rasaiah, R. Lynden-Bell and S. Lee, *J. Phys. Chem. B*, 1998, **102**, 4193–4204.
74 K. B. Møller, R. Rey, M. Masia and J. T. Hynes, *J. Chem. Phys.*, 2005, **122**, 114508.
75 R. E. Larsen, W. J. Glover and B. J. Schwartz, *Science*, 2010, **329**, 65–69.
76 F. Uhlig, O. Marsalek and P. Jungwirth, *J. Phys. Chem. Lett.*, 2012, **3**, 3071–3075.
77 K. Carter-Fenk, B. A. Johnson, J. M. Herbert, G. K. Schenter and C. J. Mundy, *J. Phys. Chem. Lett.*, 2023, **14**, 870–878.
78 T. Quickenden and J. Irvin, *J. Chem. Phys.*, 1980, **72**, 4416–4428.
79 H. Iglev, A. Trifonov, A. Thaller, I. Buchvarov, T. Fiebig and A. Laubereau, *Chem. Phys. Lett.*, 2005, **403**, 198–204.